

SCIENTIFIC REPORTS



OPEN

Programmable Deployment of Tensegrity Structures by Stimulus-Responsive Polymers

Received: 1 March 2017

Accepted: 26 April 2017

Published online: 14 June 2017

Ke Liu¹, Jiangtao Wu², Glaucio H. Paulino¹ & H. Jerry Qi²

Tensegrity structures with detached struts are naturally suitable for deployable applications, both in terrestrial and outer-space structures, as well as morphing devices. Composed of discontinuous struts and continuous cables, such systems are only structurally stable when self-stress is induced; otherwise, they lose the original geometrical configuration (while keeping the topology) and thus can be tightly packed. We exploit this feature by using stimulus responsive polymers to introduce a paradigm for creating actively deployable 3D structures with complex shapes. The shape-change of 3D printed smart materials adds an active dimension to the configurational space of some structural components. Then we achieve dramatic global volume expansion by amplifying component-wise deformations to global configurational change via the inherent deployability of tensegrity. Through modular design, we can generate active tensegrities that are relatively stiff yet resilient with various complexities. Such unique properties enable structural systems that can achieve gigantic shape change, making them ideal as a platform for super light-weight structures, shape-changing soft robots, morphing antenna and RF devices, and biomedical devices.

Deployable structures have important applications, such as space structures^{1–3}, robotics^{4, 5}, morphing antenna and RF devices⁶, and biomedical devices⁷. Integrated only by self-stress, tensegrity^{8, 9} structures are inherently deployable^{1, 10, 11}. They do not require mechanisms to lock the deployed shape, as many other deployable systems do, because the self-stresses also provide structural stability^{12, 13}. As the struts are connected by flexible cables, complex articulated joints that are typical in truss-made or origami-inspired deployable structures are also circumvented. These features apply to both terrestrial^{11, 14} and outer-space structures^{1, 15}, scaling from nanometers¹⁶ to meters². Beyond deployability, tensegrity displays aesthetic formation⁸, high-precision controllability and easy tunability^{11, 14}. In nature, tensegrity structures are found in living systems and play an important role to the fundamental structure and function of cells^{17, 18}.

Recently, advanced additive manufacturing technologies using active materials, such as shape memory polymers (SMP)^{19–22}, hydrogels²³ or composites²⁴, have provided the capability to print shape-evolving products, and thus adds time as the fourth dimension to the printed structures, or 4D printing. Among active materials, SMPs exhibit excellent recoverability, easy tailoring of properties. More recently, 3D printing SMPs become available, making them a good fit for fabricating active structural systems with complicated geometries.

Here, we use 3D printed thermally responsive SMPs to create actively deployable tensegrities. Thanks to the aforementioned unique properties of tensegrity, our paradigm for creating self-deployable structures distinguishes itself from related attempts for reconfigurable structures^{20–25} in many aspects, such as superior volume expansion, design simplicity, resilience after deployment, and modularity. Figure 1A shows schematically the overall concept and the details of the design. The struts, which are made of SMP and are straight in their permanent shape, can be programmed into compact shapes. They are then connected by elastic cables (Fig. 1A-a). Once the assembly is heated, the struts recover their original straight shapes. However, because of constraints imposed by the cables, self-stresses are generated in both cables and struts, and the loosely connected struts and cables can stand up and form a fully functional 3D tensegrity structure (Fig. 1A-b).

¹School of Civil and Environmental Engineering, Georgia Institute of Technology 5142B Jesse W. Mason Building, 790 Atlantic Drive NW, Atlanta, GA, 30332, USA. ²George W. Woodruff School of Mechanical Engineering, Georgia Institute of Technology 801 Ferst Drive MRDC 4104, Atlanta, GA, 30332, USA. Ke Liu and Jiangtao Wu contributed equally to this work. Correspondence and requests for materials should be addressed to G.H.P. (email: paulino@gatech.edu) or H.J.Q. (email: qih@me.gatech.edu)

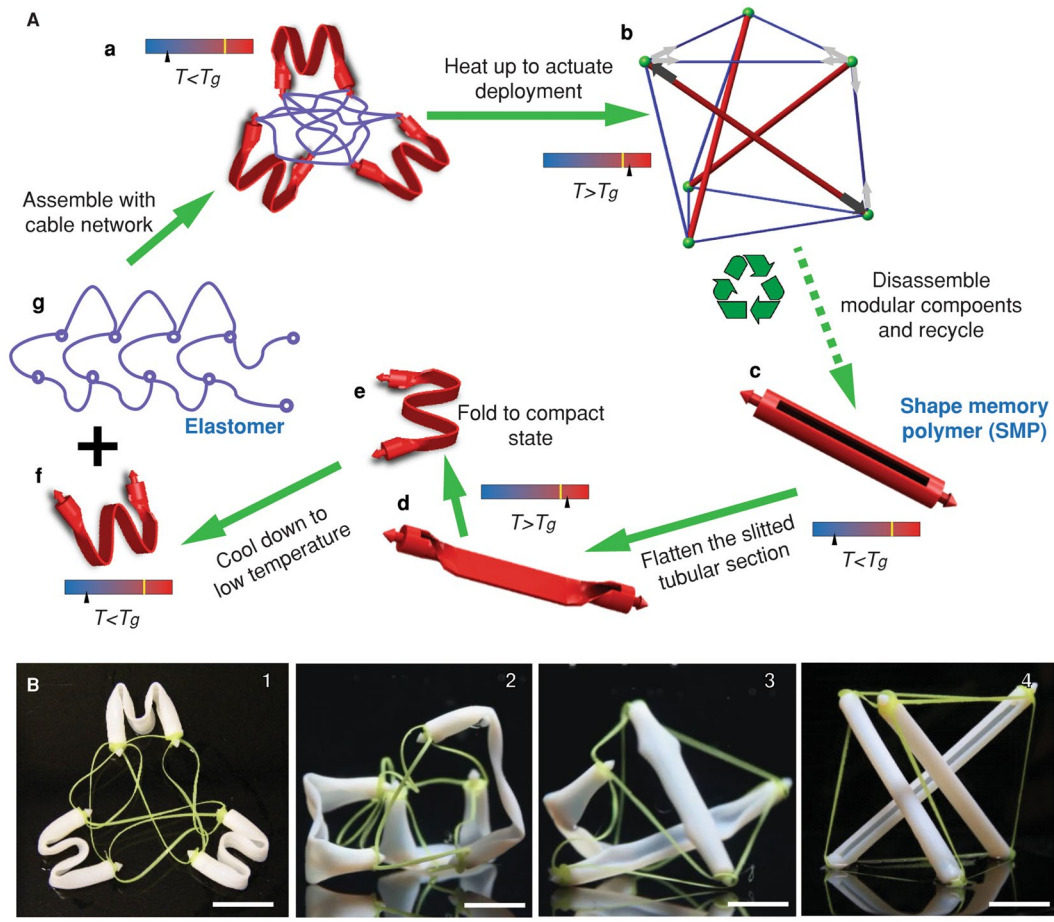


Figure 1. Procedure for creating an active tensegrity. Deployment of an active tensegrity is based on the shape recovery property of shape memory polymers (SMP). (A) Schematic of the overall concept and design. (a) The struts, which are programmed to compact shapes, are connected by a network of elastomer cables. (b) Upon heating, the recovery of the struts to their straight shapes leads to actuation of the structure to a 3D resilient tensegrity structure. To achieve this concept, (c) the struts are designed to have tubular shapes with longitudinal slit portions and are 3D printed using SMPs; (d,e) the SMP struts are folded into compact shapes at a temperature that is above the glass transition temperature (T_g) of the SMP; (f) decreasing the temperature below T_g fixes the struts in the compact shapes, which are then assembled with the elastomer cables (g) according to the topology of the design to form a loose assembly (a); heating the assembly to a temperature above T_g leads the struts to their original shapes, and thus the constraints from the cables induce self-stress. As a consequence, a stable tensegrity structure is obtained. (B) The experimental result shows the deployment process. The scale bars represent 15 mm.

Results

Design and Demonstration. To realize the aforementioned concept, we design the struts and cables and use 3D printing to implement our designs – Fig. 1A shows design details. The struts have tubular shapes with slit central portions so that they can be easily packed by bending (Fig. 1A–c). The two ends of the struts are designed with arrowheads to help mounting the cable network. Struts are printed by an acrylate-based photopolymer, named Verowhite, which is one of the model materials in our multimaterial 3D printer (Objet 260 Connex) and is a SMP with the glass transition temperature (T_g) around 60 °C^{19, 25}. The printed struts are then heated to a temperature (65 °C) above its T_g for programming. We first flatten the central portion (Fig. 1A–d) then bend it into a W-shape to enable favorable compaction (Fig. 1A–e). Finally, we lower the temperature to 10 °C and the struts are fixed in the W-shape (Fig. 1A–f). For the cables, because they form a continuous network^{12, 14}, we design them (Fig. 1A–g) according to the structural topology and print them using an FFF (Fused Filament Fabrication) printer with Filaflex, which is a stretchable elastomeric filament material. The nodes in the cable network are designed with small holes so that they match the arrowheads of the struts. Finally, we attach the cable network with programmed struts (Fig. 1A–a). Up to this step, the tensegrity structure gains its topology but not its geometry; it is unconstrained in configuration and thus could be tightly packed into an arbitrary shape. We then increase the temperature to deploy the structure. Fig. 1B and Movie S1 show the deployment when the assemblage is thrown into a tank of hot water at ~65 °C. As the struts recover their original straight shapes, cables are stretched and self-stresses grow within the system. This renders “life” to our tensegrity, i.e. it stands up, to reach its designated geometry, resulting in a giant configurational change, although it had never been built to this shape before.

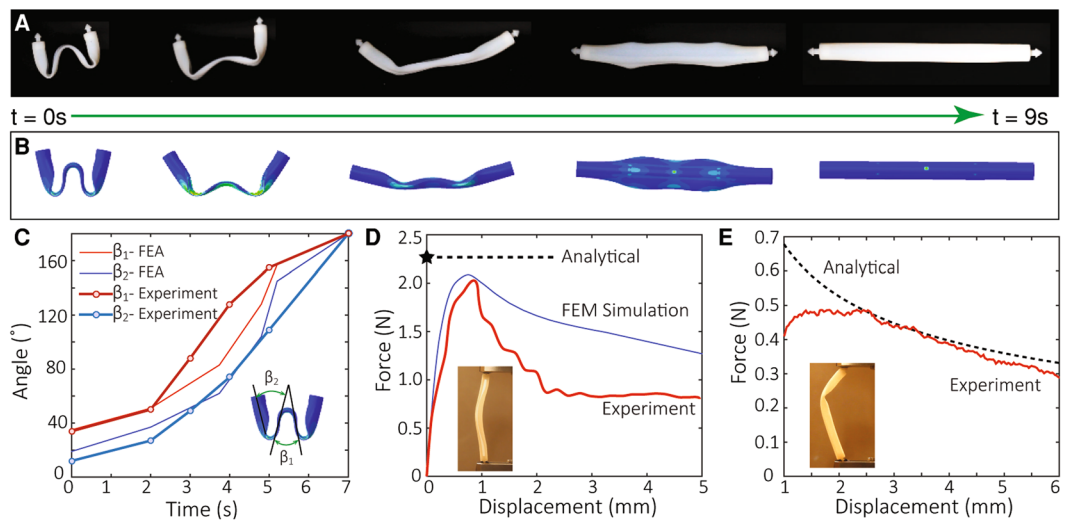


Figure 2. Properties of the slotted tubular struts via 3D printing. (A) The snapshot images of the free recovery sequence of a strut at 65 °C. (B) The predictions from the corresponding finite element method (FEM) simulation. (C) The opening angles of the strut during the free recovery and the comparison with the FEM simulation. The inset shows the definitions of the two opening angles. (D) The critical load of a single strut during uniaxial compression from the experiment and the FEM simulation. The inset shows the experimental setup. Considering the boundary condition in the experimental setup, a 0.75 effective length ratio gives the upper bound on the critical buckling load of a single strut. In practical designs, because the joints in our tensegrity are almost free in rotation, 1.0 effective length shall be used. (E) The critical load of a single strut during its recovery. Derivation for the analytical prediction is elaborated in SI. In the experiment, a small initial displacement (1 mm) is imposed to prevent the opened cross section from closing.

Theoretical Analysis. The mismatch between the initial lengths of the struts and cables is critical for determining the self-stresses, which in turn dictate if the deployment can be successful and the stiffness of the tensegrity is enough (see SI for details). In general, neither too small nor too large self-stresses can deploy the structure. This is because too small self-stresses would not provide enough stiffness to support the total weight, but too large self-stresses would prevent the strut from a full recovery. Therefore, it is important to design proper initial lengths. Toward this end, we conduct theoretical analysis of the self-stress generated during and after the strut recovery to gain insight (see SI). We also conduct finite element (FE) simulations to confirm our theoretical analysis. Fig. 2A and B show the comparison between the experiment and the FE simulation of the shape change of a strut during a free recovery (Movie S2). Fig. 2C shows the opening angles (defined in the inset) measured during the recovery. Overall, the FE simulation results match the experiments reasonably well. The difference mainly comes from the uncertainty from experimental measurement, which is a challenge due to the dynamic nature of the free recovery. To estimate the maximum self-stress beyond which a deployed strut will buckle, we conduct a compression test to measure the critical force (Fig. 2D). In addition, by using the effective length ratio of 0.75, the estimated buckling load derived using the Euler buckling criteria is close to those in the experiment and the FE simulation (see SI). The FE simulation shows relatively large deviation after the peak force is reached because instability occurs in the post-buckling regime. Nonetheless, the peak force is the most important design parameter. Fig. 2E compares the theoretical estimation and the experimental result of the critical force in the strut during the recovery, i.e. when the cross-section is open. The critical force for a strut during its recovery is typically smaller than the Euler buckling load after its recovery. On one hand, the different cross-sections lead to different elastic buckling loads. On the other hand, the energy level of deformation state before the buckling is high, so the system quickly buckles into the post-buckling state, which is a more energetically favorable state. Nevertheless, during the recovery, the system is driven by its internal energy following a low energy path, which gives a lower force. This difference in the buckling force and the recovery force is beneficial; this is because the low recovery force makes the recovery relatively easy and the high buckling force can prevent the deployed tensegrity structure from buckling.

Hence, for our design of struts, the critical force shown in Fig. 2E determines whether a strut can successfully deploy when assembled in the tensegrity system. Based on the theoretical and FE analyses, we choose the initial lengths to be 70 mm for the strut, 49 mm for the horizontal cables, and 45 mm for the tilted cables (see SI). This design yields a maximum compression force in the struts to be 0.15 N, about half of the minimum critical force (i.e. the recovery force) of the strut. A compression test is applied on the final structure. By matching the initial stiffness with theoretical predictions, we can inversely determine the magnitude of the induced self-stresses. We achieve approximately a maximal compression in the struts around 0.20 N, larger than the designed value, but still less than the critical forces.

Reduced Degree-of-Freedom Design and 3D Structures. In our design, the cables are loose before deployment and the folded struts are free to move in space. Such excessive degrees-of-freedom may lead to incorrect positioning of struts and may create the risk of cable entanglement, or trap the structure at an undesirable

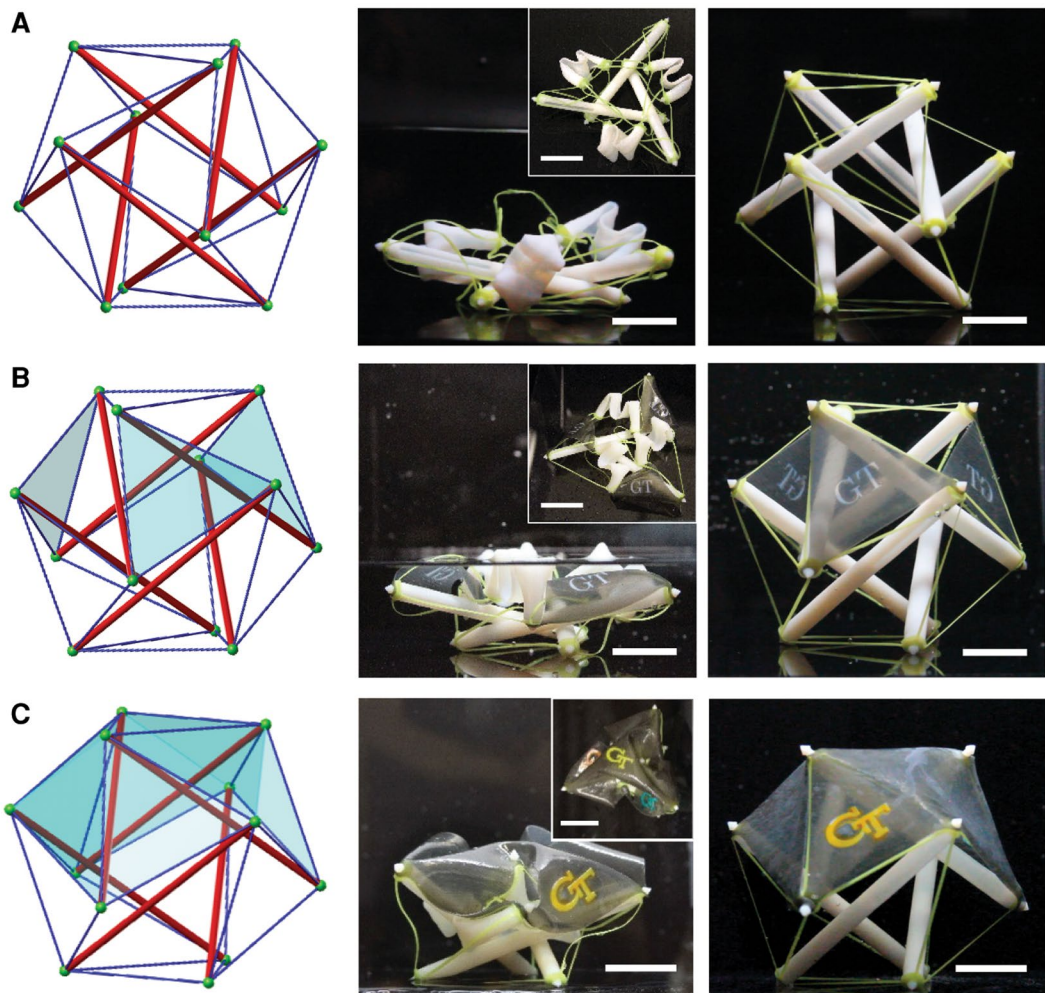


Figure 3. Deployment of 6-strut spherical tensegrity. **(A)** Deployment of a spherical tensegrity using the partial folding strategy to improve reliability of deployment. **(B)** Positioning of three discrete pieces of surfaces into space. **(C)** Deployment of a continuous surface supported by the active tensegrity to form a tent. The resultant structural system mimics the fundamental structure of vertebrates, with the membrane as skin, elastic cables as muscles, and relatively rigid struts as the skeleton (biomimetics). The scale bars represent 15 mm.

configuration by (Fig. S7). To overcome such drawback, we reduce the degrees-of-freedom of the undeployed structure. One approach is to take advantage of the decoupled hierarchies and reduce the number of packed struts, i.e., leaving some struts straight. In this way, the tensegrity deployment becomes more deterministic, while the structure can still be stored in a compact state that occupies much less space than its deployed configuration. This design concept is illustrated by the 6-strut spherical tensegrity shown in Fig. 3A, where three of the struts are deprogrammed and are made partially solid to have an eccentric center of gravity, which stabilize the structure against gravity as it stands up. Such a design leads to successful deployment (Movie S3).

Our active tensegrity can be used to form 3D structures with surfaces that can serve as a platform to host functional devices. As a demonstration, we attached elastomer membranes (Fig. 3B and C) on the previous 6-strut tensegrity. On both discrete and continuous surfaces (Fig. 3B and C, respectively), we printed the “GT” (Georgia Tech) logo; it is not hard to imagine that one can print electronic circuits, to take advantage of the gigantic shape-change and to enable functionalities of the structure. Movie S4 and S5 show the deployment processes. The configuration of the deployed surfaces depends on the base tensegrity. With some state-of-art form-finding approaches for tensegrity^{26–28}, we can generate space covering surfaces of almost any geometry. In addition, the attached surfaces increase the reliability of the deployment, as they provide additional constraints and reduce arbitrariness during the deployment.

Sequential Deployment. The development of digital materials in 3D printing allows us to print parts using polymers with different T_g 's, thus offering different shape memory characteristics that permit sequential shape changes^{20,29}. We take advantage of the digital SMPs and program the deployment sequence to further pursue complex tensegrities in a controlled manner. Here, we choose three SMPs: DM-1 with T_g around 37 °C; DM-2 with T_g around 57 °C; and the SMP used in the above (Verowhite, termed as BM here) with T_g around 60 °C (see SI). We first create one 2-layer prismatic tower tensegrity (Fig. 4A), and one 3-layer tensegrity^{1,30} (Fig. 4B), by using DM-1

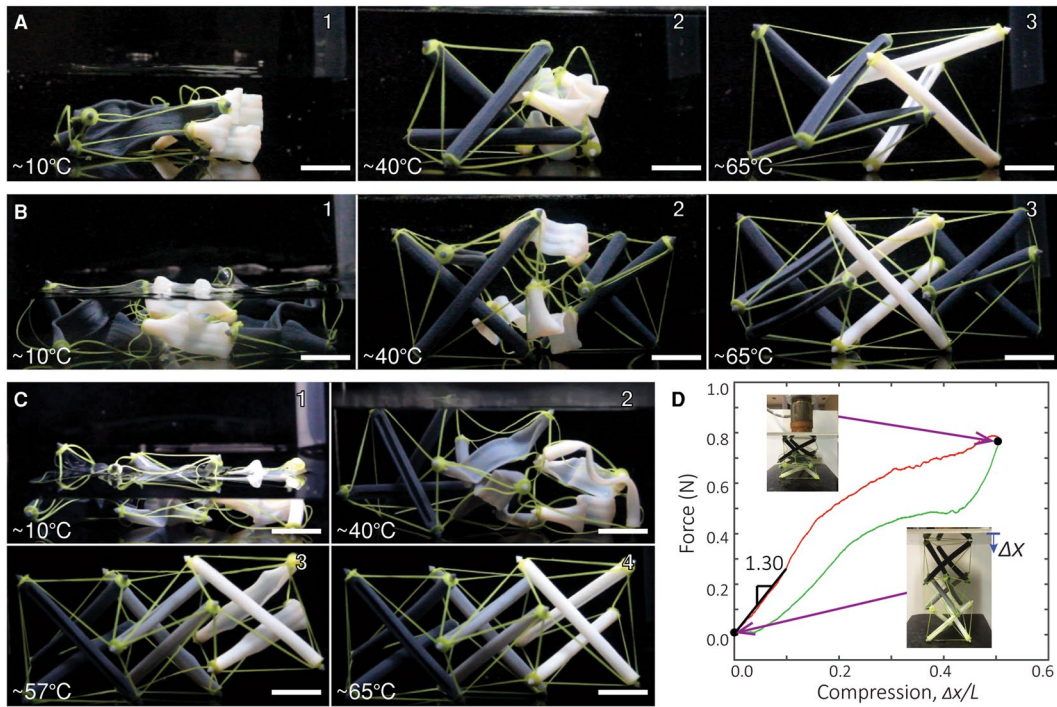


Figure 4. Programmed deployment of layered tensegrity structures. (A) Programmed deployment sequence of the 2-layer tensegrity using 2 different SMPs for the struts [DM-1 (the dark grey material) and BM (the white material)]. (B) Programmed deployment sequence of the 3-layer tensegrity using 2 different SMPs for the struts [DM-1 (the dark grey material) and BM (the white material)]. The two end layers have struts made with SMP of a lower T_g than the middle layer. (C) Programmed deployment sequence of the 3-layer tensegrity using 3 different SMPs for the struts. The three SMPs have increasing T_g 's from left to right. The darker the color, the lower the T_g . (D) Compression test of the deployed 3-layer tensegrity made with 3 different SMPs. The test reveals a maximum compression in the struts around 0.12 N. The scale bars represent 15 mm.

and BM, to demonstrate the capability of the programmed deployment. The struts with different materials are programmed in the same manner as shown in Fig. 1. They are then assembled with the elastomer cable networks. Fig. 4A–1 and B–1 show the unactuated shapes of the structures. As there are no self-stresses, they lay on the ground. To activate the structure, we first increase the temperature to 40 °C by submerging the structure in a hot water bath. As shown in Fig. 4A–2 and B–2, the struts made by DM-1 recovered first, forming partially deployed tensegrity structures, with the right and middle parts not activated in Fig. 4A–2 and B–2, respectively. Finally, we increase the temperature to 65 °C to deploy the struts made with the BM, as shown in Fig. 4A–3 and B–3. The deployments of the two tensegrities are recorded in Movies S6 and S7.

To further demonstrate control over the deployment sequence, we prepare a three-layer structure with DM-1 DM-2, and BM (Fig. 4C). To deploy the structure, we increase the temperature in three steps: first to 40 °C, then to 57 °C and finally to 65 °C. Fig. 4C–2 to C–4 shows the sequential deployment (Movie S8). Because the glass transition temperatures of DM-2 and BM are close, the distinction between the actuations of the middle layer and the right layer are not very clear; better distinction can be achieved if more digital materials were available with more distinguishable T_g s.

Mechanical Behaviors of Tensegrity. The obtained tensegrity structures allow elastic deformation to a significant amount of magnitude without fracture or yielding. Figure 4D shows a compression test of the 3-layer structure in Fig. 4C. Since the stiffness of the cables is much lower than the struts (see SI), the global deformation of the tensegrity is mainly carried by local deformation of the elastomer cables. The plateau in the loading curve and the small dip in the unloading curve in Fig. 4D are caused by the inherent multi-stability feature of this tensegrity design. By matching the initial stiffness with theoretical predictions (Fig. S1), we can inversely approximate the magnitude of induced self-stresses. The calculation and estimation for other tensegrity structures in Fig. 4 can be found in Fig. S8.

Discussion

The tensegrity in our design paradigm consists of *two hierarchies*: the *first hierarchy* is the compaction and recovery of individual struts; the *second hierarchy* is the final geometry of the tensegrity, i.e. the global structure. Therefore, the final configurational change is composed of both material-induced shape change and topology-induced shape change. The *second hierarchy* amplifies the *first hierarchy* to achieve gigantic volume expansions. Furthermore, these two hierarchies are decoupled, i.e. the final tensegrity does not depend on how we design and compact the strut (the *first hierarchy*). Therefore, other designs of the struts, such as different

cross-section shapes or programmed shapes can be used. In this paper, our design of each strut is inspired by the storable tubular extendable member (STEM)³¹ usually used on satellites. Such a design provides a relatively high critical force after recovery. The slit design enables favorable deployments. However, this is not the only design alternative and thus one can design the strut based on other considerations^{20, 23, 24}. As shown above, we avoid specialized design and dedicated fabrication for every new active structure, but can apply components of the same design to create different structures by varying combinations, in a way similar to the LEGO toy, which opens a new venue that allows for quick fabrication of 3D active structures through modular designs. We can also recycle the struts to save material and reduce waste.

In retrospect, we create a method for realizing active tensegrity by combining 3D printing with actuation to deploy 3D structures that respond to environmental stimuli. Our paradigm of active tensegrity is unique and novel as it integrates the complementary features of tensegrity structures and smart materials, merging the frontiers of structural mechanics and material science. The intriguing properties of tensegrity allows the active deployment to have two decoupled hierarchies: programming the SMP struts into compact shapes, and the topology of the actual tensegrity. Such a decoupling strategy leads to gigantic shape change, allows for modular design, and provides rich programmability and tunability. The struts are allowed to have other shapes and be programmed into a compact shape so that they can be assembled with the elastomer cables according to the topology of the tensegrity. The active tensegrity structures can be programmed to deploy in a sequential fashion by differentiating the glass transition temperatures of the SMPs used for the struts. Further enrichment includes, for example, using shape memory composites²² to achieve finer control of shape change, or using materials such as hydrogels^{23, 24} to design the structure to respond to different types of environmental stimuli. In addition, surfaces, which could be used as a platform for integrating functionality, can be attached to the nodes in the tensegrity to enable active devices with dramatic property changes. Therefore, our paradigm of active tensegrity offers a platform for generic devices/applications that can benefit from the gigantic shape changes reported in the present research. With unique properties of tensegrity and remote controllable actuation by temperature, we can foresee the great potential of active tensegrity in various applications. For example, tensegrity structures have been successfully exploited as deployable antenna and reflectors on satellites, for example, contractile reflector for a small satellite that can be packaged within an envelope^{32, 33}. Another application is the tensegrity robot for locomotion and duct systems^{34, 35}. In addition, Carpentieri *et al.* recently provides a method to use the minimal mass deployable tensegrity for solar energy harvesting on water canals³⁶. These traditional applications of tensegrity usually need mechanical drivers to deploy. Now, empowered by SMP, the active tensegrity structure is self-deployable, with the capability to adapt automatically to environmental changes. The active tensegrity may also be applied for biomedical purpose, such as stent^{7, 37, 38}. A stent is a type of flexible tubular device for minimally invasive surgery. It is capable of being folded into small dimensions and then deployed to open up a blocked lumen. The active tensegrity could be suitable for self-deployable stent which deploys under human body temperature once inserted. There are various tensegrity designs that approximate tubular shapes¹². In addition, as we showed in this paper (Fig. 4D, Fig. S8), deployed active tensegrity structures have great resilience to undergo large elastic deformations, which is a desired feature for biomedical devices so that the stent can also adapt to the deformation of human tissues.

Methods

Sample fabrication. The slotted tubular struts were fabricated using an Objet 3D printer (Objet 260 Connex, StrataSys Inc, Eden Prairie, MN, USA) in digital material mode using the PolyJet technology. The printer can combine two base materials, using pre-determined ratios to make the so-called digital materials. The digital materials differ in mechanical and thermal properties. The curable liquid photopolymer was jetted onto the build tray and then cured by UV polymerization. The three digital materials used in this paper are Verowhite plus, DM9895 (DM-1) and DM8530 (DM-2) in Stratasys material library. The cables were fabricated using the Fused Filament Fabrication (FFF) technology on a HYREL 3D Printer (System 30 M, Hyrel 3D Inc, Norcross, GA, USA). A rubbery material named Filaflex (Recreus, Elda, Spain) was used, which is a thermoplastic elastomer base polyurethane. The extruder was especially equipped with a dual drive system to fulfill the task of printing flexible filaments. The filament was melted at ~232 °C and deposited through a nozzle of 500 µm diameter onto the tray. The cable nets were printed by two passes of reversed orientation. The extrusion paths were optimized to ensure the quality of the printing.

Deployment control. A water temperature control system was built, which includes a glass water tank, a DC hot water pump, a water heater, an electrical thermometer, and plastic tubes. The tank held some cold water (~10 °C) at the beginning of each experiment. The level of the cold water submerged the undeployed tensegrity assemblies. To activate the deployment, hot water (~95 °C) was pumped from the water heater into the tank to increase the temperature of the cold water, which is monitored by an electrical thermometer. In the programmed deployment test, we stopped injecting hot water once the water reached the desired temperature. After the whole tensegrity deployed, we were able to drain the water from the tank.

Compression tests of the deployed tensegrity. We performed the compression tests of the deployed tensegrity structures using an electromechanical universal material test machine (MTS Criterion® Series 40, Eden Prairie, MN, USA) at room temperature (~25 °C). The deployed tensegrity was placed on a flat stage and then compressed by another flat plate mounted to the load cell. The stage and plate were lubricated to reduce friction. The compression loading rate was set to be 0.2 mm/s. The forces and displacements were recorded at a 10 Hz sampling rate, and a load cycle was performed. The unloading commenced when the global deformation (compression) reached half the height of the tensegrity.

References

1. Tibert, G. *Deployable Tensegrity Structures for Space Applications* PhD thesis, Royal Institute of Technology (2002).
2. Tibert, G. & Pellegrino, S. Deployable Tensegrity Masts. *44th AIAA/ASME/ASCE/AHS/ASC Structures, Structural Dynamics, and Materials Conference*, 1–10, doi:[10.2514/6.2003-1978](https://doi.org/10.2514/6.2003-1978) (2003).
3. Pellegrino, S. Deployable Structures. (Springer-Verlag Wien, 2001).
4. Caluwaerts, K. *et al.* Design and control of compliant tensegrity robots through simulation and hardware validation. *Journal of The Royal Society Interface* **11**, 1–13, doi:[10.1098/rsif.2014.0520](https://doi.org/10.1098/rsif.2014.0520) (2014).
5. Moored, K. W., Kemp, T. H., Houle, N. E. & Bart-Smith, H. Analytical predictions, optimization, and design of a tensegrity-based artificial pectoral fin. *International Journal of Solids and Structures* **48**, 3142–3159, doi:[10.1016/j.ijsolstr.2011.07.008](https://doi.org/10.1016/j.ijsolstr.2011.07.008) (2011).
6. Liu, X., Yao, S., Cook, B. S., Tentzeris, M. M. & Georgakopoulos, S. V. An origami reconfigurable axial-mode bifilar helical antenna. *IEEE Transactions on Antennas and Propagation* **63**, 5897–5903, doi:[10.1109/TAP.2015.2481922](https://doi.org/10.1109/TAP.2015.2481922) (2015).
7. Kuribayashi, K. *et al.* Self-deployable origami stent grafts as a biomedical application of Ni-rich TiNi shape memory alloy foil. *Materials Science and Engineering A* **419**, 131–137, doi:[10.1016/j.msea.2005.12.016](https://doi.org/10.1016/j.msea.2005.12.016) (2006).
8. Heartney, E. & Snelson, K. D. *Kenneth Snelson: Forces Made Visible*. (Hudson Hills, 2009).
9. Snelson, K. D. The Art of Tensegrity. *International Journal of Space Structures* **27**, 71–80 (2012).
10. Hanaor, A. Debunking “Tensegrity” - A Personal Perspective. *International Journal of Space Structures* **27**, 179–183, doi:[10.1260/0266-3511.27.2-3.179](https://doi.org/10.1260/0266-3511.27.2-3.179) (2012).
11. Motro, R. *Tensegrity: Structural Systems for the Future*. (Elsevier, 2006).
12. Zhang, J. & Ohsaki, M. *Tensegrity Structures - Form, Stability, and Symmetry*. (Springer Japan, 2015).
13. Calladine, C. R. Buckminster Fuller’s “Tensegrity” structures and Clerk Maxwell’s rules for the construction of stiff frames. *International Journal of Solids and Structures* **14**, 161–172, doi:[10.1016/0020-7683\(78\)90052-5](https://doi.org/10.1016/0020-7683(78)90052-5) (1978).
14. Skelton, R. E. & de Oliveira, M. C. *Tensegrity Systems*. (Springer, 2009).
15. Zolesi, V. S. *et al.* In 42nd International Conference on Environmental Systems International Conference on Environmental Systems (ICES) (American Institute of Aeronautics and Astronautics, 2012).
16. Liedl, T., Höglberg, B., Tytell, J., Ingber, D. E. & Shih, W. M. Self-assembly of three-dimensional prestressed tensegrity structures from DNA. *Nature nanotechnology* **5**, 520–524, doi:[10.1038/nnano.2010.107](https://doi.org/10.1038/nnano.2010.107) (2010).
17. Ingber, D. E. The architecture of life. *Scientific American* **278**, 48–57 (1998).
18. Scarff, G. *Biotensegrity: The structural basis of life*. (Handspring Publishing, 2014).
19. Ge, Q., Qi, H. J. & Dunn, M. L. Active materials by four-dimension printing. *Applied Physics Letters* **103**, doi:[10.1063/1.4819837](https://doi.org/10.1063/1.4819837) (2013).
20. Mao, Y. *et al.* Sequential Self-Folding Structures by 3D Printed Digital Shape Memory Polymers. *Scientific Reports* **5**, 13616, doi:[10.1038/srep13616](https://doi.org/10.1038/srep13616) (2015).
21. Raviv, D. *et al.* Active printed materials for complex self-evolving deformations. *Scientific Reports* **4**, 7422, doi:[10.1038/srep07422](https://doi.org/10.1038/srep07422) (2014).
22. Wu, J. *et al.* Multi-shape active composites by 3D printing of digital shape memory polymers. *Scientific Reports* **6**, 24224, doi:[10.1038/srep24224](https://doi.org/10.1038/srep24224) (2016).
23. Gladman, S. A., Matsumoto, E. A., Nuzzo, R. G., Mahadevan, L. & Lewis, J. A. Biomimetic 4D printing. *Nature Materials* **15**, 413–418, doi:[10.1038/nmat4544](https://doi.org/10.1038/nmat4544) (2016).
24. Mao, Y. *et al.* 3D Printed Reversible Shape Changing Components with Stimuli Responsive Materials. *Scientific Reports* **6**, 24761, doi:[10.1038/srep24761](https://doi.org/10.1038/srep24761) (2016).
25. Ge, Q., Conner, K. D., Qi, H. J. & Martin, L. D. Active origami by 4D printing. *Smart Materials and Structures* **23**, 094007 (2014).
26. Tachi, T. In *Advances in Architectural Geometry 2012* (eds Lars Hesselgren *et al.*) 259–268 (Springer Vienna, 2013).
27. Li, Y., Feng, X.-Q., Cao, Y.-P. & Gao, H. A Monte Carlo form-finding method for large scale regular and irregular tensegrity structures. *International Journal of Solids and Structures* **47**, 1888–1898 (2010).
28. Zhang, J. Y. & Ohsaki, M. Adaptive force density method for form-finding problem of tensegrity structures. *International Journal of Solids and Structures* **43**, 5658–5673 (2006).
29. Xie, T. Recent advances in polymer shape memory. *Polymer* **52**, 4985–5000, doi:[10.1016/j.polymer.2011.08.003](https://doi.org/10.1016/j.polymer.2011.08.003) (2011).
30. Sultan, C. Modeling, design, and control of tensegrity structures with applications PhD thesis, Purdue University (1999).
31. Rimrott, F. P. J. Storable Tubular Extendible Member. *Machine Design* **37**, 156–165 (1965).
32. Tibert, A. G. & Pellegrino, S. Deployable Tensegrity Reflectors for Small Satellites. *Journal of Spacecraft and Rockets* **39**, 701–709, doi:[10.2514/2.3867](https://doi.org/10.2514/2.3867) (2002).
33. Tibert, G. *Deployable Tensegrity Structures for Space Applications* PhD thesis, Royal Institute of Technology (2002).
34. Kim, K. *et al.* Rapid Prototyping Design and Control of Tensegrity Soft Robot for Locomotion. *IEEE International Conference on Robotics and Biomimetics* **2014**, 7–14 (2014).
35. Friesen, J. *et al.* DuCTT: A Tensegrity Robot for Exploring Duct Systems. *IEEE International Conference on Robotics and Automation (Icra) 2014*, 4222–4228 (2014).
36. Carpentieri, G., Skelton, R. E. & Fraternali, F. A minimal mass deployable structure for solar energy harvesting on water canals. *Structural and Multidisciplinary Optimization* **55**, 449–458, doi:[10.1007/s00158-016-1503-5](https://doi.org/10.1007/s00158-016-1503-5) (2016).
37. Htay, T. & Liu, M. W. Drug-Eluting Stent: A Review and Update. *Vascular Health and Risk Management* **1**, 263–276 (2005).
38. Huo, L. *et al.* Single-Junction Organic Solar Cells Based on a Novel Wide-Bandgap Polymer with Efficiency of 9.7. *Adv Mater*, doi:[10.1002/adma.201500647](https://doi.org/10.1002/adma.201500647) (2015).

Acknowledgements

K.L. and J.W. contributed equally to this work. G.H.P. and K.L. acknowledge the support of the NSF award (CMMI-1538830). H.J.Q. and J.W. acknowledge the support of an AFOSR grant (FA9550-16-1-0169; Dr. B.-L. “Les” Lee, Program Manager) and NSF awards (EFRI-1240374, CMMI-1462894, CMMI-1462895), K.L. acknowledges support from the China Scholarship Council. We are also grateful for the endowment provided by the Raymond Allen Jones Chair at the Georgia Institute of Technology. The information provided in this paper is the sole opinion of the authors and does not necessarily reflect the views of the sponsoring agencies.

Author Contributions

K.L. and J.W. made equal contributions in conducting experiments, theoretical development and simulations. G.H.P. and H.J.Q. provided the research idea and its conceptual development. All the authors participated in manuscript writing and reviewed the manuscript.

Additional Information

Supplementary information accompanies this paper at doi:[10.1038/s41598-017-03412-6](https://doi.org/10.1038/s41598-017-03412-6)

Competing Interests: The authors declare that they have no competing interests.

Publisher's note: Springer Nature remains neutral with regard to jurisdictional claims in published maps and institutional affiliations.



Open Access This article is licensed under a Creative Commons Attribution 4.0 International License, which permits use, sharing, adaptation, distribution and reproduction in any medium or format, as long as you give appropriate credit to the original author(s) and the source, provide a link to the Creative Commons license, and indicate if changes were made. The images or other third party material in this article are included in the article's Creative Commons license, unless indicated otherwise in a credit line to the material. If material is not included in the article's Creative Commons license and your intended use is not permitted by statutory regulation or exceeds the permitted use, you will need to obtain permission directly from the copyright holder. To view a copy of this license, visit <http://creativecommons.org/licenses/by/4.0/>.

© The Author(s) 2017

Supporting Information

Programmable Deployment of Tensegrity Structures by Stimulus-Responsive Polymers

Ke Liu¹, Jiangtao Wu¹, Glaucio H. Paulino, H. Jerry Qi**

¹These authors (K. Liu and J. Wu) contributed equally to this work.

K. Liu, Prof. G. H. Paulino

School of Civil and Environmental Engineering, Georgia Institute of Technology

5142B Jesse W. Mason Building, 790 Atlantic Drive NW, Atlanta, GA 30332, USA

E-mail: paulino@gatech.edu

J. Wu, Prof. H. J. Qi

George W. Woodruff School of Mechanical Engineering, Georgia Institute of Technology

801 Ferst Drive MRDC 4104, Atlanta, GA 30332, USA

E-mail: qih@me.gatech.edu

Materials and Methods

Material characterization: A dynamic mechanical analysis (DMA) machine (Model Q800, TA Instruments Inc, New Castle, DE, USA) was used to characterize the mechanical and thermomechanical properties of the materials. The viscoelastic properties of the printed SMPs were measured in the film tension mode. The material samples (dimension 10mm×3mm×1mm) were first heated to 90°C on the DMA machine and stabilized for 10 minutes to reach thermal equilibrium. A preload of 0.001N was applied to straighten the samples. During the DMA tests, the strain of the samples was controlled to oscillate at a frequency of 1 Hz with a peak strain amplitude of 0.1%. Meanwhile, the temperature decreased from 90°C to 0°C with a rate of 2°C/min. The glass transition temperature T_g is identified by the temperature when the viscoelastic loss tangent ($\tan\delta$) reaches its peak value. The T_g 's of the three strut materials are 60°C (BM: Verowhite plus), 37°C (DM-1: DM9895), and 57°C (DM-2: DM8530).

The stress-strain behavior of the cable material was tested in controlled force mode on the DMA machine at room temperature ($\sim 25^\circ\text{C}$). A complete load cycle was performed at a very low speed (quasi-static) on a sample with dimensions $10\text{mm} \times 0.9\text{mm} \times 0.25\text{mm}$. The printed sample was stretched to 3.1 MPa at loading rate of 0.5 MPa/min and then unloaded. The initial tangent elastic modulus was determined to be 16.43MPa from the stress strain curves (see Figure S5).

Supporting Text

S1. Analysis of self-stressed tensegrity structures

Based on the design, linear analysis of self-stressed tensegrity helps us to correlate the initial tangent stiffness of the tensegrity structure to its self-stress level. Considering the small strain due to self-stress, we treat the strut material as linear elastic and take the initial modulus for the calculation to simplify the design process. The governing equation takes the form of a linear equation $\mathbf{K}\mathbf{u} = \mathbf{F}$, where \mathbf{K} is the stiffness matrix, \mathbf{u} contains the nodal displacements, and \mathbf{F} contains the applied forces. Due to the self-stress, the stiffness matrix for a tensegrity structure is different from a normal truss structure^{1,2}. The major difference is the additional contribution of the geometrical stiffness matrix \mathbf{K}_G . Thus the tangent stiffness matrix takes the form:

$$\mathbf{K} = \mathbf{K}_E + \mathbf{K}_G, \quad (\text{S1})$$

where, \mathbf{K}_E is the linear stiffness matrix. For completeness, we summarize the derivation of \mathbf{K}_G here. Assume that for a member (either a cable or strut) i , its two nodes, length and self-stress induced force are a , b , L_i and T_i , respectively. We define the components of a connectivity matrix \mathbf{C} as:

$$C_{ij} = \begin{cases} 1, & \text{if member } i \text{ is connected to node } j, \text{ and } j = a \\ -1, & \text{if member } i \text{ is connected to node } j, \text{ and } j = b \\ 0, & \text{otherwise} \end{cases} \quad (\text{S2})$$

We also define a diagonal matrix \mathbf{Q} such that:

$$Q_{ii} = T_i / L_i . \quad (\text{S3})$$

The ratio T_i / L_i is known as the force density². Let $\bar{\mathbf{T}}$ be the normalized self-stress induced force vector with maximum compression in struts equal to 1. Denoting γ as a scaling factor (which equals to the maximum compressive force in struts), we can rewrite \mathbf{Q} as:

$$\mathbf{Q} = \gamma \bar{\mathbf{Q}}, \quad (\text{S4})$$

where $\bar{Q}_{ii} = \bar{T}_i / L_i$. Because $\bar{\mathbf{T}}$ is an intrinsic property of a tensegrity design, it is a constant vector. Thus, we can write the so-called force density matrix² as:

$$\mathbf{E} = \mathbf{C}^T \mathbf{Q} \mathbf{C} = \gamma \mathbf{C}^T \bar{\mathbf{Q}} \mathbf{C}. \quad (\text{S5})$$

Since the strains of the members caused by the self-stress are small, the geometric stiffness matrix can be expressed as:

$$\mathbf{K}_G = \mathbf{E} \otimes \mathbf{I}_{3 \times 3} = \gamma \bar{\mathbf{K}}_G. \quad (\text{S6})$$

Finally, with the contribution of the linear stiffness matrix, the stiffness matrix of the tensegrity structure can be approximated for small deformation as:

$$\mathbf{K}(\gamma) = \mathbf{K}_E + \gamma \bar{\mathbf{K}}_G. \quad (\text{S7})$$

From the above derivation, we can see that the stiffness matrix of a tensegrity is a function of its self-stress level γ . We find that the higher the self-stress, the stiffer the tensegrity. Using this equation, we can find the relationship between the initial tangent modulus of a tensegrity under global uniaxial compression and the self-stress level γ . The initial tangent modulus is the ratio of the applied force over the compression magnitude (in terms of displacement). Figure S1 plots the curve of initial tangent modulus versus self-stress level, based on the material properties for 3 tensegrity designs. The tangent modulus shown here is calculated using the non-dimensional

displacements, which is the downward compression displacements normalized by the heights of the tensegrity designs, and thus, the unit of the tangent modulus is in Newton (N). The two 3-layer tensegrities (with different materials) yield almost identical curves, so only one is plotted for clarity. This curve does not start from (0,0) because the 3-layer tensegrity is kinematically determinate, thus its stiffness matrix is not singular when there is no prestress ($\mathbf{K}(0)=\mathbf{K}_E$). According to the experimental compression tests of the active tensegrities, we can approximate the initial tangent modulus of a tensegrity. Then, based on the curves shown in Figure S1, we can inversely estimate how much self-stress we have successfully applied to the active tensegrity.

S2. The two critical loads for the slitted tubular struts

From the previous section, we can see that the (initial) stiffness of a tensegrity structure depends on the self-stress level. However, the achievable self-stress level of an active tensegrity is not arbitrary, as it is determined by two critical factors. *The first factor is that the compression on struts should not prevent their full recovery.* In the final stage of deployment, some SMP struts in the active tensegrity will be subject to compression before full recovery, with their tubular cross-section still open. *The second critical factor is that, after deployment, the struts should not buckle under the self-stress compression.* If the struts buckle, then the tensegrity will lose some self-stress and cannot completely reach the designated shape. In the following, we will derive analytical estimations of these two critical strut loads. We first compute the critical force during the recovery, when the tubular cross section of a strut is open, as shown in Figure S2a. We make the following assumptions: *(1) a tube can be analyzed using shell theory because the thickness is relatively small; (2) the mid-surface is subject to isometric deformation; (3) the static behavior of the SMP can be regarded as elastic when the temperature is fixed and the strain is relatively small.* The meaning of the symbols used in the derivation is illustrated in

Figure S2. Therefore, supposing that the changes in the curvatures along the two principle directions are $(-1/r, 1/R)$, we can write the total strain energy at the bending region as³:

$$U_B = \frac{D\alpha R\psi}{2} \left(\frac{1}{r} + \frac{r}{R^2} - \frac{2\nu}{R} \right). \quad (\text{S8})$$

The symbol D denotes the flexural rigidity, defined as:

$$D = \frac{Et^3}{12(1-\nu)}, \quad (\text{S9})$$

where E is Young's modulus and ν is Poisson's ratio. The value of r is determined when U_B is minimized³. Therefore, $r=R$. Then the bending moment is calculated as:

$$M = \frac{\partial U_B}{\partial \psi} = D\alpha(1-\nu). \quad (\text{S10})$$

At the final stage of the strut's recovery, a single kink about a quarter from the end of a strut is usually observed (see Movie S3). Thus, we can draw the shape schematically as shown in Figure S2c. The regions that are not opened are much stiffer than the bending region. Therefore, we may treat those regions as rigid. Notice that,

$$\lambda L \sin \theta_1 = (1-\lambda)L \sin \theta_2. \quad (\text{S11})$$

If the two applied forces are aligned along the same line, then equilibrium is obtained as:

$$M = F_{cr} (\lambda L \sin \theta_1 + R \cos \theta_1). \quad (\text{S11})$$

Thus the critical force can be calculated by:

$$F_{cr} = \frac{M}{\lambda L \sin \theta_1 + R \cos \theta_1} \geq \frac{Et^3 \alpha}{12(\lambda L \theta_1 + R)}, \quad (0 < \theta_1 < \pi/2). \quad (\text{S11})$$

In our case, the typical value for λ is around 0.25. The angle θ_1 can be computed from the deformed length of the strut $(\lambda L \cos \theta_1 + (1-\lambda)L \cos \theta_2)$. The equality holds when θ_1 is small. The later expression is used because it is simple and conservative. The derivation requires a portion with fully opened cross section along the strut (which forms a "kink"), thus it is not accurate

when the strut is almost straight (i.e. ϱ_i becomes very small), because in reality the opened cross section starts to enclose before the strut recovers to straight, so the deformation mode no longer has a “kink”.

The critical load before the buckling of the struts after deployment is given by the Euler buckling formula⁴,

$$F_{buckling} = \frac{\pi^2 EI_{min}}{L_{eff}^2}. \quad (\text{S12})$$

The effective length L_{eff} depends on the boundary conditions of the strut. In the compression tests, the fixture of the sample constrains the free rotation at the two ends, resulting in an effective length around $0.75L$. However, in the tensegrity, the two ends are assumed to be pinned, and thus $L_{eff} = L$. The minimum static moment of inertia I_{min} is determined to be the static moment of inertia of the X - X axis at the geometric centroid GC , which is denoted as I_{GC-XX} ,

$$I_{GC-XX} = R^3 t \left[\frac{\alpha}{2} + (\alpha - \pi) \frac{\sin^2(\alpha/2)}{(\alpha/2)^2} + \frac{\sin \alpha}{2} \right]. \quad (\text{S13})$$

We note that, in the experiment, the struts are not loaded at the geometric center (GC) of the cross section. Instead, the compressive forces are loaded at point O (at the center of the mid-surface circle). As a consequence, the actual critical buckling force will be lower than the estimation, since the buckling mode involves a combination of bending and twisting.

S3. Design of cables

As explained in our paper, the self-stress in the tensegrity is induced by prescribed length differences between cables and struts. We assume that after successful deployment, the struts become straight and their deformation under compression is negligible (recall that the struts are much stiffer than the cables). Therefore, we control the level of self-stress magnitude by

manipulating the initial length of cables. We did this for two reasons. First, we do not want the initial length of cables to be too long so that the deployed tensegrity cannot gain enough self-stress to become stable and stiff. Second, the initial lengths of cables should not be so short that the struts cannot recover during deployment or stay straight after deployment, due to the excessive self-stress magnitude.

Suppose that the desired self-stress level is γ and member i is a cable. Given the normalized force vector $\bar{\mathbf{T}}$ (as defined in Section S1), we can determine the initial length of a cable as:

$$l_0 = \frac{d - 2\delta}{(\gamma \bar{T}_i) / (AE_c) + 1} + 2\delta. \quad (\text{S14})$$

In this equation, l_0 denotes the initial length, d is the design length of the cables which is pulled from the geometry of the tensegrity design, $\gamma \bar{T}_i$ is the desired tension in the cable, A is the cross-sectional area of the cable, and δ is the ineffective length at each end of a cable which changes very little. Considering the contact angles of cables and struts, δ is generally 1.4~3 times the distance d shown in Figure S3. Typically, the force is small, and we can assume linear behavior for the cables. Hence the initial elastic modulus E_c is used.

Such calculation provides an approximate guide for determining the initial lengths of cables based on the value of γ , which needs to be greater than 0, but less than the minimum critical load of the strut. In reality, the control of the self-stress level and final geometry will not be precise due to many practical factors, for example: the twisting of cables, the plasticity of the cable material, the printing accuracy, and the entanglement of the cables near the joints. In some cases, adjustment based on the experimental results is needed, especially for tensegrity designs with complex geometries.

S4. Detailed experimental analysis

The shape recovery behavior of the strut comes from the viscoelastic properties of the SMPs. The DMA tests are performed to investigate the viscoelastic properties of the printed strut materials. The storage modulus and loss tangent $\tan \delta$ vs. temperature plots of the printed three strut materials are shown in Figure S4.

The Filaflex material exhibits rubber-like viscoelastic properties at room temperature. Uniaxial tension tests are performed to investigate the mechanical properties of the printed Filaflex material. The stress vs. strain curve is shown in Figure S5. The specimen occupies the same cross section as the cables, which is a rectangle of 250 μm -thick and 920 μm -wide. The uniaxial stretch is up to ~40% of the initial length.

S5. Constitutive model for the SMP

The multi-branch model is used to describe the viscoelastic properties of the printed SMP materials. In this model, one elastic equilibrium branch and several thermo-viscoelastic non-equilibrium branches are arranged in parallel. The non-equilibrium branch is described by the Maxwell element, represented by a viscous damper and an elastic spring connected in series. The total stress of the material can be expressed as:

$$\sigma_{total} = \sigma_{Eq} + \sum_{m=1}^n \sigma_{non}^m = E_{Eq} e + \sum_{m=1}^n E_{non}^m \int_0^t \frac{\partial e}{\partial s} \exp \left[- \int_s^t \frac{dt'}{\tau_m(T)} \right] ds, \quad (\text{S15})$$

where E_{Eq} is the Young's modulus of the equilibrium branch and both E_{non}^m and τ_m are the Young's modulus and temperature dependent relaxation time of the m -th non-equilibrium branch. To consider the temperature effects, the time temperature superposition principle (TTSP) is used. The relaxation time τ_m at temperature T can be calculated using the relaxation time τ_m^R at the reference temperature, given by:

$$\tau_m(T) = a^{shift}(T) \tau_m^R, \quad (S16)$$

where $a^{shift}(T)$ is the time temperature superposition shifting factor. According to O'Connell and McKenna⁵, the shifting factors can be calculated by combining the Williams-Landel-Ferry (WLF) equation⁶ and the Arrhenius-type equation⁷. If the temperature is higher than the reference temperature, the shifting factor can be expressed using the WLF equation:

$$\log[a^{shift}(T)] = -\frac{C_1(T - T_{ref})}{C_2 + (T - T_{ref})}, \quad T > T_{ref}. \quad (S17)$$

The parameters C_1 , C_2 and T_{ref} are material parameters to be characterized by experiments. We denote A , F_c , and k^{Boltz} as the material constant, configurational energy, and Boltzmann's constant, respectively. When the temperature is lower than the reference temperature T_{ref} , the shifting factor is expressed by the Arrhenius-type equation:

$$\ln[a^{shift}(T)] = -\frac{AF_c}{k^{Boltz}} \left(\frac{1}{T} - \frac{1}{T_{ref}} \right), \quad T < T_{ref}. \quad (S18)$$

The parameters including E_{eq} , E_m^{non} , τ_m^R , C_1 , C_2 and AF_c/k^{Boltz} are determined from the DMA tests. The storage modulus at high temperature (90°C for BM, 65°C for DM-1, 85°C for DM-2) is the equilibrium modulus E_{eq} for each of the materials. For the multi-branch model, the temperature dependent storage modulus $E_s(T)$, loss modulus $E_l(T)$ and loss tangent $\tan\delta(T)$ can be respectively computed by:

$$E_s(T) = E_{eq} + \sum_{m=1}^n \frac{E_m^{non} \omega^2 [\tau_m(T)]^2}{1 + \omega^2 [\tau_m(T)]^2}, \quad (S19a)$$

$$E_l(T) = \sum_{m=1}^n \frac{E_m^{non} \omega \tau_m(T)}{1 + \omega^2 [\tau_m(T)]^2}, \quad (S19b)$$

$$\tan \delta(T) = \frac{E_l(T)}{E_s(T)}. \quad (\text{S19c})$$

The symbol ω denotes the test frequency. By employing a nonlinear regression software ^{8,9}, the parameters E_m^{non} , τ_m^R , C_1, C_2 and AF_c/k can be determined by fitting the $\tan \delta$ and storage modulus from experimental DMA tests. The material parameters used in this paper are provided in Table S1.

To show the capability of this model, the comparison of the DMA curves between the experiment and the simulation are shown in Figure S6. We can see that the multi-branch model explains the thermomechanical behavior of the printed strut materials in the temperature range used for programming and actuation processes.

S6. Finite element analysis

The recovery process and mechanical properties of struts are modeled using the FEA software ABAQUS (Simulia, Providence, RI, USA). The hybrid C3D8RHT element is used. We implement the multi-branch model based on Prony's series, which is defined as:

$$G(t) = G_{Eq} + \sum_{m=1}^n G_m e^{-t/\tau_m}, \quad (\text{S20})$$

where G is the total shear modulus, G_{Eq} and G_m are the shear modulus of the equilibrium branch and m -th non-equilibrium branches. Applying the incompressible condition, the shear modulus G is calculated as $G_m = E_m/3$, where E_m is the elastic modulus from the multi-branch model. The material parameters for the multi branch model are elaborated upon in Section S5. To apply the temperature effects, the shift factors are calculated using the WLF equation and Arrhenius-type equation^{6,7}. The UTRS subroutine is used to implement the WLF equation and Arrhenius-type equation.

Considering the symmetry of the strut and boundary conditions, only 1/4 of a strut is used for simulation of free recovery. The slit of the strut is first opened into a nearly flat configuration in the middle part of the strut at 65°C, which is above the T_g of the BM (Verowhite). The pressure used to open the slit is applied on the inner surface of the slit near the opening. After the slit is opened, we fix the middle section of the strut (one end in the 1/4 model) and add a pressure load on the end of the strut and in the transverse direction of the strut to bend it into a “U”-shape. To further deform the strut into the “W”-shape, we fix the 1/4 section of the strut and apply pressure at the end in the opposite direction of the previous step. After the deformation process is finished, we cool the temperature to 25°C, at which the material is in a glassy state. Then all the external loading and constraints are removed, and the deformed shape of the strut is “frozen” due to viscoelasticity. To simulate the recovery process, the temperature is increased to 65°C. The recovery process by the simulation is compared with the experimental results, as shown in Figure 2.

The strut under compression is also modeled to determine the after-recovery critical force ($F_{buckling}$). In this simulation, the whole strut is modeled to consider asymmetric deformation modes. We impose an ambient temperature of 65°C. One end of the strut is pinned in directions x, y, z within the central zone (radius of 1mm), creating a partially fixed end. At the other end, the center zone is pinned in x, y directions (partially fixed), and a displacement load of rate 0.25mm/s is applied in the $-z$ direction. This boundary condition is similar to the case of the strut compression experiment, but more restrictive than the actual boundary condition as embedded in the tensegrity structures.

A similar procedure can be applied to predict the mechanical performance of struts made with various SMPs.

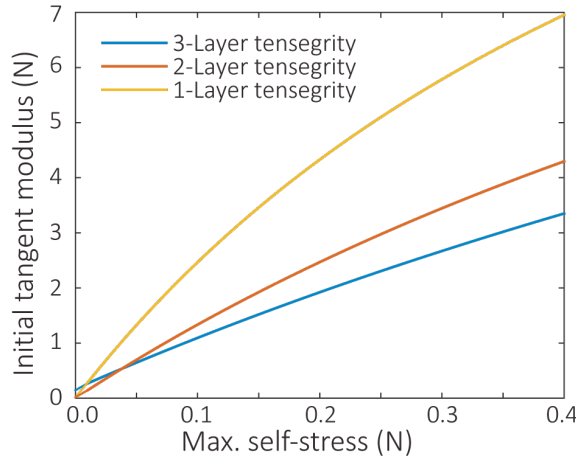


Figure S1. Initial tangent modulus vs. maximum self-stress forces in struts.

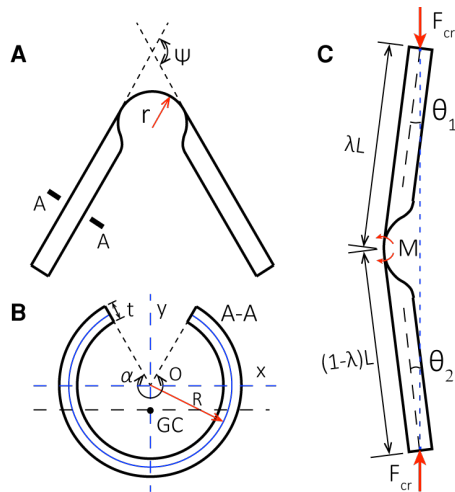


Figure S2 (A) Schematic of a folded strut with opened cross section. (B) Cross section (A-A) of the struts. (C) Sketch of the critical scenario in the recovery of struts (during the deployment of an active tensegrity), based on observations from the experiments.

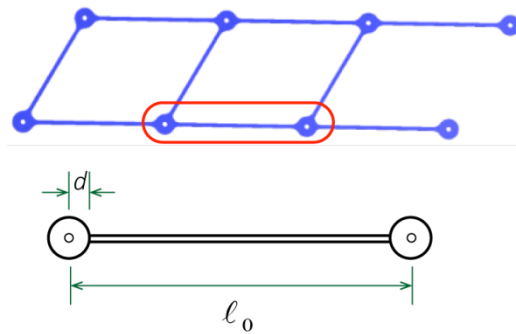


Figure S3 Schematic of the cable network design.

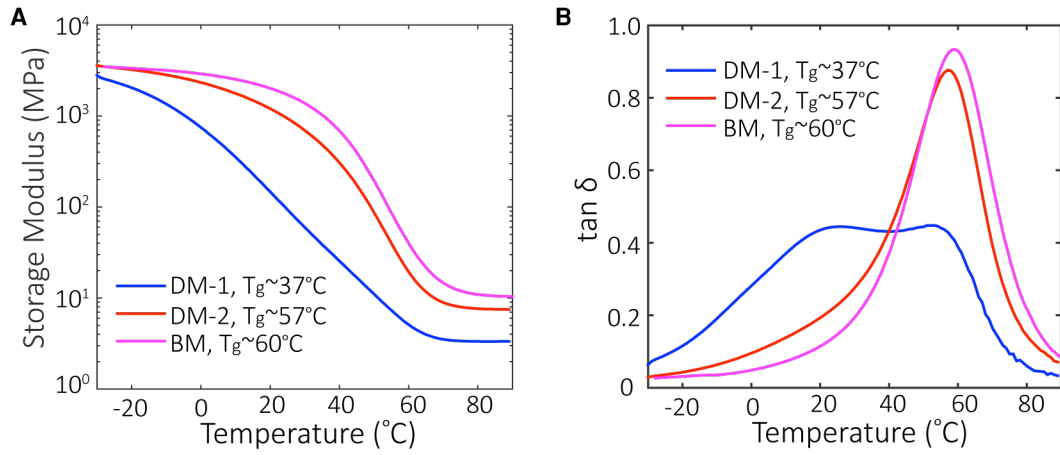


Figure S4 (A) Storage modulus vs. temperature curves for three SMPs. (B) Loss tangent $\tan \delta$ vs. temperature curve.

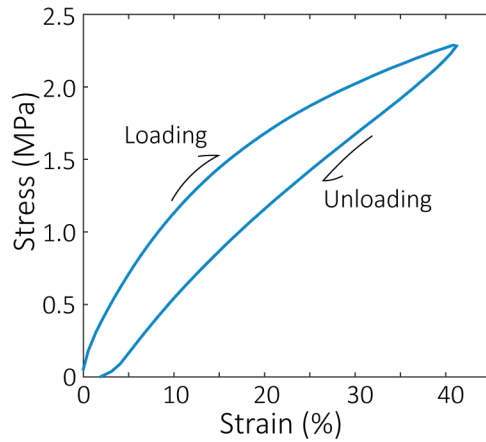


Figure S5 The stress-strain curve of Filaflex material at room temperature (~25°C).

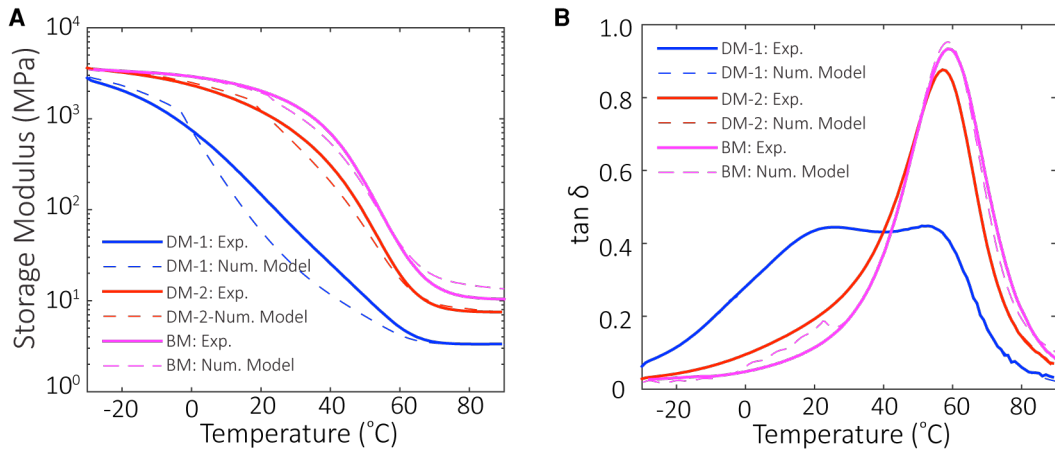


Figure S6 Comparison of the DMA curves between experimental data and numerical models for three SMP materials used in this paper.

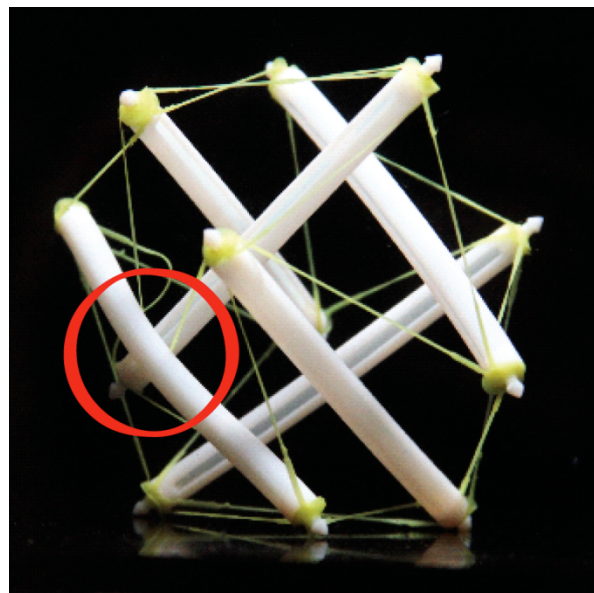


Figure S7 Failed deployment of a 6-strut spherical tensegrity, due to physical contact between struts, as highlighted by the red circle. As discussed in the main text, when the cables are loose, the folded struts are almost free to move in space. In this example, a strut blocks the recovery of another strut.

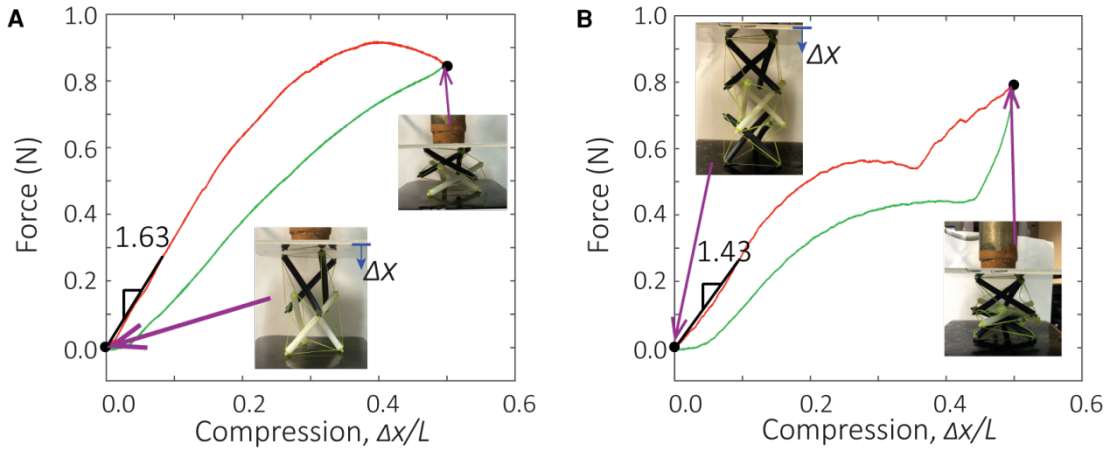


Figure S8 The compression tests on the two-layer tensegrity and the three-layer tensegrity, whose struts are made with two SMPs. (A) Compression test of the resultant deployed 2-layer tensegrity using 2 different SMPs for struts (BM and DM-1). The red line indicates the loading process while the green line indicates the unloading process. Estimated maximal compression equals 0.12N. (B) Compression test of the deployed 3-layer tensegrity made with 2 different SMPs (BM and DM-1). Maximal compression in the struts is estimated to be around 0.14N. The three-layer tensegrity shows two dips in both the loading and unloading process. This is due to the inherent multi-stability behavior of such structures. That is, the structure has a multiple local minima of stored energy at different configurations. For example, when one layer of the tower is fully flattened, the structure is at an alternative stable state (other than the fully deployed configuration). Due to the contact of struts, the other stable configurations cannot be reached. However, it still leads to a reduction in stiffness of the structure (snap through). The 3-layer tensegrity in B illustrates this effect more clearly than the one in Figure 4D of the main content because the structure in A has more DM-1 struts, which are less stiff than DM-2 and BM struts in room temperature ($\sim 25^\circ\text{C}$). Thus, when a contact between struts happens, the DM-1 struts will bend, leading the structure slightly closer to the ideal alternative stable configuration, although this state cannot be fully reached.

Table S1.

Material parameters for the multi branch model.

	Verowhite		DM9895		DM8530	
Branch	E _{non} (MPa)	τ _i	E _{non} (MPa)	τ _i	E _{non} (MPa)	τ _i
E ₁	148.7076	2.00E-08	300	0.0001	170	1E-07
E ₂	119.7517	4.27E-07	275	0.000657	188	9.93E-07
E ₃	131.9798	5.47E-06	296	0.003872	212	0.00001
E ₄	147.1372	5.89E-05	305	0.02	239	9.08E-05
E ₅	282.3444	0.000547	350	0.1	268	0.00074
E ₆	320.9668	0.004524	378	0.576863	293	0.005374
E ₇	354.2126	0.032439	292	3.401616	308	0.035368
E ₈	427.2871	0.2	215	20	291	0.2
E ₉	178.2132	1	147	96.82391	285	0.954957
E ₁₀	143.8276	3.250259	95.213467	362.9461	138	3.182197
E ₁₁	151.2221	9.451896	63.12765	1000	162	7.497457
E ₁₂	162.8788	30.23741	62.0921	2671.527	178	25.11365
E ₁₃	162.4149	100	52.099306	7912.87	153	87.11596
E ₁₄	151.456	315.2367	42.374719	23498.79	133	283.7953
E ₁₅	141.8913	927.9366	35.205449	71461.38	122	905.6253
E ₁₆	111.7587	8849.219	27.897552	228551.6	112	3025.975
E ₁₇	140.7818	2849.202	20.760769	726401	98.09554	10000
E ₁₈	81.89721	25294.7	15.532429	2277776	83.26095	32677.22
E ₁₉	52.68197	72900	11.281878	7091525	65.70456	96510.16
E ₂₀	12.47854	653520.3	8.305791	21997171	59.12021	267333.4
E ₂₁	28.03173	213000	5.959708	68236585	51.92218	773277.7
E ₂₂	1.712558	5370000	4.351312	2.08E+08	44.76933	2339554
E ₂₃	4.830405	2000000	3.329757	6.41E+08	34.59949	7613180
E ₂₄	1.197657	85400000	2.644468	2.07E+09	21.72712	26070126
E ₂₅	1.383214	20000000	2.196711	7.07E+09	9.995279	1E+08
E ₂₆	0.000183	3.61E+08	1.578065	2.4E+10	2.916758	5.22E+08
E ₂₇	2.537188	2E+09	0.1070122	1E+11	0.957138	5.77E+09
E _{eq} (MPa)	10.4		3.30		7.5	
T _g (°C)	60		38		57	
T _{ref} (°C)	22		-3		17	
C1	17.44		17.44		17.44	
C2	66.35		42.1		50.5	
AF _c /k	-23000		-23000		-24000	

Movie S1 Deployment of a 3-strut tensegrity.

Movie S2 Numerical simulation of the free recovery of a single strut with the slotted tubular cross section.

Movie S3 Deployment of a 6-strut spherical tensegrity, using the partial folding strategy.

Movie S4 Deployment of a 6-strut spherical tensegrity with 3 discrete attaching pieces of surface.

Movie S5 Deployment of a 6-strut spherical tensegrity with one continuous attaching piece of surface.

Movie S6 Programmed sequential deployment of a 2-layer tower tensegrity, whose struts are made with 2 SMPs.

Movie S7 Programmed sequential deployment of a 3-layer tower tensegrity, whose struts are made with 2 SMPs.

Movie S8 Programmed sequential deployment of a 3-layer tower tensegrity, whose struts are made with 3 SMPs.

References:

- 1 Guest, S. D. The stiffness of prestressed frameworks: A unifying approach. *International Journal of Solids and Structures* **43**, 842-854, doi:10.1016/j.ijsolstr.2005.03.008 (2006).
- 2 Zhang, J. & Ohsaki, M. *Tensegrity Structures - Form, Stability, and Symmetry*. (Springer Japan, 2015).
- 3 Calladine, C. R. The theory of thin shell structures 1888-1988. *ARCHIVE: Proceedings of the Institution of Mechanical Engineers, Part A: Power and Process Engineering 1983-1988 (vols 197-202)* **202**, 141-149, doi:10.1243/PIME_PROC_1988_202_020_02 (1988).
- 4 Timoshenko, S. P. & Gere, J. M. *Theory of Elastic Stability*. 2nd edn, (Dover Publications, 2009).
- 5 O'Connell, P. A. & McKenna, G. B. Arrhenius-type temperature dependence of the segmental relaxation below Tg. *The Journal of Chemical Physics* **110**, 11054, doi:10.1063/1.479046 (1999).
- 6 Williams, M. L., Landel, R. F. & Ferry, J. D. The Temperature Dependence of Relaxation Mechanisms in Amorphous Polymers and Other Glass-forming Liquids. *Journal of the American Chemical Society* **77**, 3701-3707, doi:10.1021/ja01619a008 (1955).
- 7 Di Marzio, E. A. & Yang, A. J. M. Configurational entropy approach to the kinetics of glasses. *J Res Natl Inst Stan* **102**, 135-157, doi:DOI 10.6028/jres.102.011 (1997).
- 8 Diani, J., Gilormini, P., Frédy, C. & Rousseau, I. Predicting thermal shape memory of crosslinked polymer networks from linear viscoelasticity. *International Journal of Solids and Structures* **49**, 793-799, doi:10.1016/j.ijsolstr.2011.11.019 (2012).

- 9 Sherrod, P. Nonlinear Regression Analysis Program, NLREG Version 5.0. *Phillip H. Sherrod, Nashville, TN* (2000).